IEEE Access
Multidisciplinary | Rapid Review | Open Access Journal

Received August 5, 2020, accepted August 11, 2020, date of publication August 14, 2020, date of current version August 26, 2020.

Digital Object Identifier 10.1109/ACCESS.2020.3016674

Outline Feature Extraction of Positron Image Based on a 3D Anisotropic Convolution Operator

TAO JIANG, MIN ZHAO, MIN YAO, RUIPENG GUO, TONG SUN, ZENGHAO ZHAO, HUI XIAO, AND YUHUI LI

College of Automation Engineering, Nanjing University of Aeronautics and Astronautics, Nanjing 210016, China
Nondestructive Detection and Monitoring Technology for High Speed Transportation Facilities, Key Laboratory of Ministry of Industry and Information Technology, Nanjing University of Aeronautics and Astronautics, Nanjing 211106, China

Corresponding author: Min Zhao (xymzhao@126.com)

This work was supported in part by the Nondestructive Detection and Monitoring Technology for High Speed Transportation Facilities, in part by the Key Laboratory of Ministry of Industry and Information Technology, in part by the Natural Science Foundation of China under Grant No. 51875289 and Grant No. 61873124, in part by the Aeronautical Science Foundation of China under Grant No. 20182952029, in part by the Fundamental Research Funds for the Central Universities under Grant No. NS2019017, and in part by the Graduate Student Innovation Projects under Grant No. kfjj20190315.

ABSTRACT This study investigates the application of positron annihilation techniques to the interior of dense metal cavities for Three-dimensional (3D) imaging and extraction of contour features inside the cavities. A feature extraction algorithm based on a 3D anisotropic convolutional operator is proposed for profile feature extraction in low-resolution, low-contrast, and low-signal-to-noise positron image. First, aiming at the problem of positron image noise caused by inconsistent detectors and metal scattering effects, an image preprocessing algorithm combining filtering and full pixel correction is proposed. A 3D anisotropic convolution operator is then designed to extract contour features. To solve the contour feature discontinuity in the extracted contour feature, a 3D path search algorithm is proposed to obtain the centroid coordinate set of the contour feature, and then the centroid coordinate set is subjected to 3D curve fitting to obtain a smooth and continuous contour feature. The study is carried out on the raw 16-bit Digital Imaging and Communications in Medicine (DICOM) data of the positron image, and the data are processed from a 3D perspective, taking full advantage of the correlation between slices in the 3D positron image. In the actual testing, positron images with different kinds of foreign objects in the cavity are extracted using a 3D anisotropic convolution operator, and the contour feature extraction resolution reaches 2 mm.

INDEX TERMS Contour feature extraction, 3D filter, 3D anisotropic convolutional operator, positron annihilation.

I. INTRODUCTION

Metal-enclosed cavity structures are widely used in aerospace and other industrial fields. Therefore, the interior cleanliness of such cavity-type structures is extremely important. Take the hydraulic system inside the landing gear of an aircraft as an example. If solid foreign objects enter this system during the pouring of hydraulic oil, then a blockage of the oil passage, a precision coupler card issue, and a small hole in the damper will occur. Next, due to the cylinder working frequently and bearing alternating loads as well as the friction between the sealing element and the inner wall, among other aspects, the inner wall of the actuating cylinder is desquamated to produce metal foreign objects mixed in the hydraulic oil. These problems will not only affect the normal and stable operation of the hydraulic system but also cause serious disasters to the aircraft. At present, the most common method to address such problems is to dismantle the hydraulic system periodically for inspection and cleaning, a process that consumes considerable manpower and material resources. Therefore, designing a method that can monitor the internal state of the hydraulic system without disassembling the hydraulic system is crucial to determine whether there are defects, foreign objects, and wear in the hydraulic system.

The positrons and negative electrons produced by the $\beta+$ decay of the radionuclide encounter an annihilation reaction, which produces a pair of high-energy gamma photons with opposite directions and 511 KeV energies. γ photons can

The associate editor coordinating the review of this manuscript and approving it for publication was Inês Domingues.

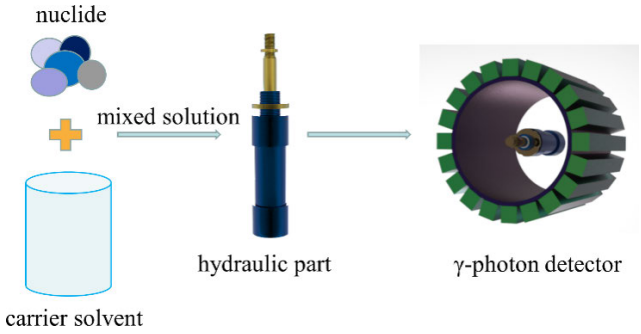

FIGURE 1. Schematic of the hydraulic part testing based on positron annihilation technology.

penetrate dense metal materials, and their annihilation process is less affected by high temperature, high pressure, and magnetic field. Therefore, the carrier solvent labeled with radionuclide is poured into the inner part of the structure under testing. Next, when the carrier solvent labeled with radionuclide releases γ photons because of $\beta+$ decay, the γ photons can be recorded by the photon detector to obtain the carrier's activity distribution image of the solvent inside the tested structural part and realize the non-destructive testing and imaging of the internal state of the closed metal cavity. Fig. 1 is a schematic of the testing.

At present, the application of positron annihilation technology to the testing of industrial fields has also achieved some good results. In 2016, Liu *et al.* [1] applied positron annihilation technology to the defect testing of an ant nest's inner cavity to solve the problem of non-destructive testing inside the irregular cavity. In 2017, Yao *et al.* [2] applied positron annihilation technology to the positron imaging testing of the combustion state inside the closed cavity and successfully observed the combustion flow field in the confined space. In 2018, Xiao *et al.* [3], [4] proposed a scattering correction algorithm to improve the quality of the reconstructed positron image after the scattering problem of the positron image inside the closed metal cavity. Chiti *et al.* [5] applied positron annihilation technology to the quantitative study of the 3D flow field inside the opaque system. The results show that positron annihilation technology can obtain accurate speeds for radial flow turbines in the entire complex 3D turbulent flow field. Bardyshev *et al.* [6] used the positron annihilation probe method to identify the presence of DEL on the internal interface of the material and estimate its energy parameters, thus correctly reflecting the contribution of the electrostatic component to the interaction between the phases and completing the double charge of the metal–polymer contact area for non-destructive testing. Cole *et al.* [7] applied positron annihilation technology to the problem of liquid distribution and content measurement in the foam flotation process. The results show that the 3D structure of the foam could be effectively measured.

With the increasing resolution of the photon detector and the optimization of the 3D image reconstruction algorithm, the use of low-dose radionuclides to test the metal cavity within a short testing time is now technically feasible. However, in industrial testing, it is difficult to obtain a positron image with high resolution, high contrast, and high signal-to-noise ratio (SNR) owing to the short testing time, the limitation of radionuclide radioactivity, the intrinsic noise of the detector, and the scattering problems within the tested metal cavity. Most of the noise in the positron image is also integrated in the feature information. Determining how to remove the noise and extract the feature information while retaining the original feature information to the maximum extent is also a difficult problem. Hence, numerous difficulties are still hindering the perfect application of positron annihilation technology to industrial non-destructive testing.

The positron image is a 3D image whose data format is 16-bit DICOM data. Compared with the 2D image, it can more accurately reflect the internal state of the device under testing. Therefore, image processing should be considered from a 3D perspective. For the noise problem in the 3D image, Zhang [8] proposed to use the gray image denoising and smoothing process commonly used in Wiener filtering to filter the noise in the strong fluctuations of the 3D point cloud image. They then combined the octree algorithm with the image and streamlined the processing of data points in the images to preserve the characteristic data points in combination with the octree algorithm. In view of the obvious speckle noise in the image because of the influence of coherence characteristics, internal circuitry of equipment components, and surrounding environment interference during ultrasound imaging, Li [9] proposed a GPU-based accelerated direct 3D non-local mean value filtering algorithm. To evaluate the suppression effect of 3D nonlinear non-uniformity filtering on high spatial resolution magnetic resonance angiography image noise, Du *et al.* [10] proposed a spatial frequency-dependent nonlinear anisotropic filtering algorithm. Zeng and Gao [11] proposed a wavelet adaptive threshold method based on Bayesian estimation to deal with the noise in the magnetic resonance image. The proposed method was able to improve the SNR. Albano [12] proposed a clustering-based roof segmentation method for the efficient and accurate segmentation of building areas and the extraction of roof features in the 3D building modeling of light detection and ranging point clouds. Nomura and Hamada [13] used the histogram of the concavity and convexity evaluation value to separate the feature edge region and showed that the proposed method can extract appropriate feature edges from 3D meshes. Zhang and Lam [14] proposed a method for detecting the edge of a 3D object by using the pupil function in an optical scanning holography system. The above research reveals that scholars have conducted extensive studies on the spatial filtering and feature extraction algorithms of 3D images and achieved good processing effects. However, the available information likewise indicates that research on 3D positron image processing for industrial testing is limited.

This paper proposes to apply the positron annihilation imaging technology to the state detection inside the closed metal cavity. Compared with the periodic manual dismantling

detection of the equipment, it greatly reduces the detection cost and improves the detection efficiency. According to the characteristics of the positron image, an appropriate filter and contour feature extraction operator are designed to process the image. The processing results show that the image processing algorithm proposed in this paper removes the noise in the positron image very well. In terms of extraction accuracy, at present, researchers have extracted the contour features in positron images at 4 mm. With the contour feature extraction algorithm in this paper, the extraction accuracy can reach 2 mm.

The contributions of this paper are as follows:

1) The 3D imaging inside the metal cavity and the extraction of contour features inside the cavity are realized by using positron annihilation technology. This paper provides new research ideas for non-destructive testing of metal cavities such as pipes and hydraulic parts in industrial equipment.
2) In this paper, two different 3D filters and full pixel correction algorithms are designed on the basis of 2D filters to solve the noise and data fluctuation problems in positron images, which are caused by detector inconsistencies and the scattering effect of γ photons, among other factors.
3) In order to extract the contour features in the positron image, this paper fully considers the problem of low contour contrast of the image edge due to the volume effect during the reconstruction of the positron image, and designs a 3D anisotropic convolution operator for contour feature extraction.

This paper is organized as follows. Section II introduces the principles of image processing algorithms. According to the noise characteristics of positron images, the filter is deduced to smooth the noise from a 3D perspective. Moreover, this section discusses the contour-type feature extraction in positron images and designs the 3D anisotropic convolution operator. In Section III, the experiment of designing multiple sets of hydraulic part verifies the feasibility of the algorithm described in Section II and of applying positron annihilation technology to the non-destructive testing of the dense metal cavity in the industry. Section IV provides the final discussion.

II. PRINCIPLES OF IMAGE PROCESSING ALGORITHMS

A. 3D IMAGE FILTERING ALGORITHM

The noise in the positron image mainly comes from the Poisson noise caused by the decay of the radioactive nuclide and the random noise caused by the inconsistent detection efficiency of the multi-channel detector, the scattering effect of γ photons, and so on. The random noise in the positron image is mainly composed of salt-and-pepper noise. Common spatial domain filters include linear and nonlinear filters. Linear weighted filters represented by Gaussian and mean filters have a good fast smoothing effect on sharp noises in the image, especially the Gaussian filter, which has good filtering effect on Gaussian noise. However, linear filters can cause image blurring, loss of detail, and edge weakness. Nonlinear filters represented by median and bilateral filters generally do not blur the image and can effectively retain the edge information of the image. Median filter has excellent filtering effect on salt-and-pepper noise in the image. When the types of noise of the positron image and the filtering characteristics of the above filters are combined, the median and bilateral filters are more in line with the requirements of positron image noise processing. In addition, after the positron image is converted from the 3D image in the DICOM data format to the 2D slice image and then filtered, the information between the slice in the positron image will be lost, resulting in an insignificant filtering effect and difficulty in smoothing the noise. Therefore, two different 3D filters, such as 3D bilateral and 3D median filters, are designed according to the noise characteristics of the positron image.

The filtering process of the 3D median filter is to sort all the pixels in the filter window according to the numerical value and then take the sorted median as the output to replace the pixel value at the center of the filter window. In weighted linear filters, the pixel value of the center pixel is the weighted average value of all pixels in its spatial neighborhood, and the weight is determined according to the spatial proximity between the neighborhood pixel and the center pixel. Bilateral filter considers the similarity of pixel values between the neighboring pixels and the central pixel on this basis, that is, the weight is determined by the similarity between the spatial proximity and the pixel value. The traditional 2D bilateral filtering is defined as follows:

$$P(x,y)=\frac{\sum_{(m,n)\in Q} I(m,n)\cdot W(x,y,m,n)}{\sum_{(m,n)\in Q} W(x,y,m,n)}, \tag{1}$$

where *(x,y)* is the coordinate of the central pixel, *P(x,y)* is the pixel value after bilateral filtering, *I(m,n)* is the neighborhood pixel in the central pixel *(x,y)* filter window Q, and W is the weight of the bilateral filter. This weight is determined by the product of spatial proximity W_d and pixel similarity W_r, as shown in the following:

$$\begin{cases} W(x,y,m,n)=W_d(x,y,m,n)\cdot W_r(x,y,m,n) \\ W_d(x,y,m,n)=e^{-\frac{(x-m)^2+(y-n)^2}{2\sigma_d^2}} \\ W_r(x,y,m,n)=e^{-\frac{\|f(x,y)-f(m,n)\|^2}{2\sigma_r^2}}, \end{cases} \tag{2}$$

where σ_d and σ_r represent the spatial proximity factor and gray-scale similarity factor, respectively. The spatial proximity factor is generally selected according to the size of the filter window, while the gray-scale similarity factor is generally selected according to the noise standard deviation of the image.

The 3D bilateral filter redefines the spatial proximity W_d on the basis of the 2D bilateral filter. The redefined spatial proximity includes the spatial proximity W_{dx} within the slice layer and the spatial proximity W_{dz} between the slice layers.

The spatial proximity W_{dx} in the slice layer is the same as the 2D spatial proximity. The spatial proximity W_{dz} between the slice layers is defined as follows:

$$\begin{cases} W_{dx}(x, y, z, m, n, o) = e^{-\frac{(x-m)^2+(y-n)^2}{2\sigma_{dx}^2}} \\ W_{dz}(x, y, z, m, n, o) = e^{-\frac{(z-o)^2}{2\sigma_{dz}^2}}, \end{cases} \tag{3}$$

where σ_{dx} is the intra-layer proximity factor, and σ_{dz} is the inter-layer proximity factor. The spatial resolution of the positron image studied in this paper is 0.5 mm $\times$ 0.5 mm $\times$ 0.5 mm. Thus, the intra-layer resolution is the same as the inter-layer resolution, that is, $\sigma_{dx} = \sigma_{dz} = \sigma_d$. Multiply W_{dx} and W_{dz} to get the 3D space proximity W_d. W_d and W_r are defined as follows:

$$\begin{cases} W_d(x, y, z, m, n, o) = e^{-\frac{(x-m)^2+(y-n)^2+(z-o)^2}{2\sigma_d^2}} \\ W_r(x, y, z, m, n, o) = e^{-\frac{\|f(x,y,z)-f(m,n,o)\|^2}{2\sigma_r^2}}. \end{cases} \tag{4}$$

To objectively compare the filtering effects of the two different 3D filters above, the images filtered by these filters are calculated and compared in terms of peak signal to noise ratio (PSNR), program running time (PTR), and structural similarity index measurement (SSIM). PSNR reflects the quality of the filtered image compared with the original image. Generally, the larger the PSNR value, the smaller the distortion after filtering and the better the filtering effect. PTR reflects the time it takes to filter the image; in industrial testing, the PTR value is required to be as small as possible in order to improve work efficiency. The present study mainly extracts the edge information and contour information in the positron image, resulting in the possible smoothing of the edges during the filtering process such that the edge is blurred. Consequently, it introduces the SSIM to evaluate the image distortion before and after filtering. SSIM is an indicator that measures the similarity of two images. It was first proposed by researchers at the University of Texas at Austin. It compares images from three aspects, namely, brightness, contrast, and structural information. The SSIM is defined as follows:

$$SSIM = l(x, y) \cdot c(x, y) \cdot s(x, y), \tag{5}$$

where x and y represent the image before and after filtering, respectively; and $l(x, y)$, $c(x, y)$, and $s(x, y)$ represent the brightness similarity, contrast similarity, and structural information before and after filtering, respectively. These similarities are mathematically defined as follows:

$$\begin{cases} l(x, y) = \dfrac{2\mu_x\mu_y + C_1}{\mu_x^2 + \mu_y^2 + C_1} \\ c(x, y) = \dfrac{2\sigma_x\sigma_y + C_2}{\sigma_x^2 + \sigma_y^2 + C_2} \\ s(x, y) = \dfrac{\sigma_{xy} + C_3}{\sigma_x\sigma_y + C_3}, \end{cases} \tag{6}$$

where μ_x and μ_y represent the mean of images x and y, respectively; σ_x and σ_y are the variances of images x and y, respectively; σ_{xy} is the covariance of images x and y; and C_1, C_2, and C_3 are the constants, which generally take $C_1 = 0.01$, $C_2 = 0.02$, and $C_3 = 0.01$.

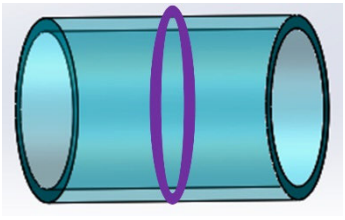

(a) Defect-free cavity

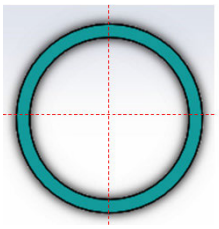

(b) Cavity section

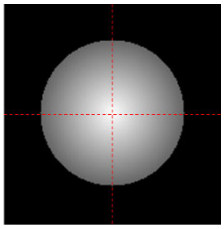

(c) Nuclide distribution

FIGURE 2. Schematic of the nuclide distribution in a defect-free cavity.

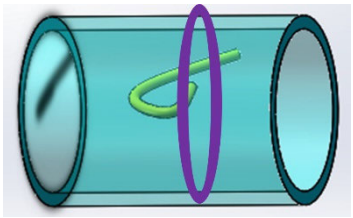

(a) Cavity containing foreign body

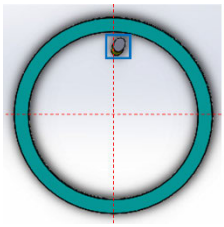

(b) Cavity section

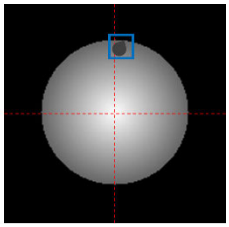

(c) Nuclide distribution

FIGURE 3. Schematic of the nuclide distribution in the cavity containing foreign bodies.

B. FEATURE EXTRACTION ALGORITHM

The positron image reflects the distribution of nuclides inside the structural part, and the different states inside the cavity affect the distribution of nuclides inside them. Fig. 2 is a schematic of the nuclide distribution in a defect-free cavity under the ideal situation of uniform distribution of nuclides. Fig. 2(a) represents a defect-free cavity, Fig. 2(b) represents the section of the purple area's cavity in Fig. 2(a), and Fig. 2(c) shows the schematic of the nuclide distribution corresponding to the section of Fig. 2(b).

Fig. 3 shows the schematic of the nuclide distribution corresponding to the presence of foreign objects in the cavity

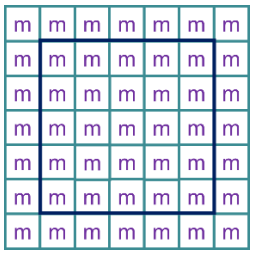

(a) Noise-free non-foreign object area

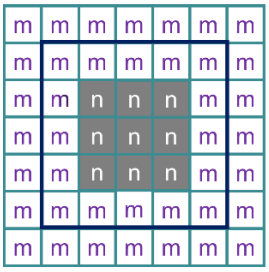

(b) Noise-free foreign object area

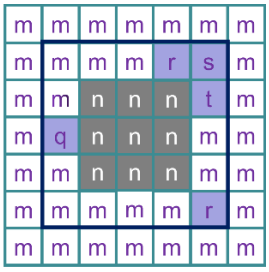

(c) Noisy foreign object area

FIGURE 4. Schematic of DICOM value distribution characteristics in the positron image.

under ideal conditions. As shown in Fig. 3(c), dark spots appear in the cavity owing to the absence of nuclides.

Figs. 2 and 3 show that when the cavity interior is in different states, the nuclide distribution in the cavity also shows different states and the DICOM values of the positron image detected present different distribution characteristics, as shown in Fig. 4.

Fig. 4(a) shows the distribution of positron image DICOM numerical values in the nuclide distribution area in Fig. 2(c) under the ideal case where the nuclide distribution is uniform and noise-free. Fig. 4(b) represents the characteristic diagram of the distribution of DICOM values in the positron image of the noiseless foreign body region in Fig. 3(c) under ideal imaging conditions, characterized by the fact that the DICOM values around the foreign body are all m, the DICOM values in the region where the foreign body is located are all n, and the size of the foreign body shown in Fig. 4(b) is 3×3. The DICOM difference between the foreign object and the surrounding pixels is (m-n). Given that no nuclide distribution appears in the region where the foreign object is located, ideally $n \ll m$, then obvious contour features will appear in the positron image. In actual testing, however, because the reconstruction process of the positron image is based on the assumption that the annihilation point has equal probability on the response line, leading to the DICOM value at the contour of the foreign object in the positron image not being $n \ll m$. Therefore, the contour in the positron image and the features are characterized by low contrast and blur. Especially when the size of the contour appearing inside the cavity is small, the scattering effect will exacerbate the blur of the contour feature and cause the contour feature to weaken. For the contour feature problem in the above positron image, the

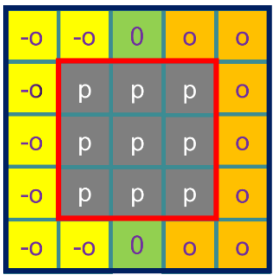

(a) Equal weight symmetry

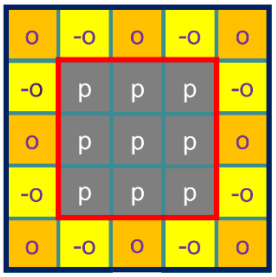

(b) Equal weight alternating

FIGURE 5. Contour feature extraction convolution kernel.

contour feature extraction convolution kernel of the positron image shown in Fig. 5(a) is designed.

The characteristics of the convolution kernel shown in Fig. 5(a) are bilateral symmetry with opposite weights, while the size of the convolution inner kernel is 3×3 and the weights are the same. Use the convolution kernel in Fig. 5(a) to perform convolution operations on the blue box areas in Figs. 4(a) and 4(b). The values after convolution are $9pm$ and $9pn$, respectively. The maximum difference between the foreign object and the surrounding pixels after the convolutional operation is $9p(m\text{-}n)$, and the contrast stretching effect of the convolved image can be changed by adjusting the weight of p. The above contour feature extraction is under the ideal condition where DICOM values around the contour are the same and noiseless. However, in actual processing, there are always noises around the contour, as shown in Fig. 4(c), which will affect the contour extraction. In response to the aforementioned problems, we transform the convolution kernel shown in Fig. 5(a) into Fig. 5(b). The weights around the convolution kernel alternate between positive and negative weights to eliminate or weaken the effect of noise around the contour on contour extraction.

Use the convolution kernels shown in Figs. 5(a) and 5(b) to perform convolution operations on the blue box areas in Figs. 4(a) and 4(c) respectively, and calculate the maximum difference between the contour and surrounding pixels. The values are $\Delta 1$ and $\Delta 2$ as follows:

$$\begin{cases} \Delta 1 = 9pm - \left\{ \begin{matrix} 9pn + o \cdot [2(r-m) + (s-m) \\ +(t-m) + (q-m)] \end{matrix} \right\} \\ \Delta 2 = 9pm - \left\{ \begin{matrix} 9pn + o \cdot [(s-m) + (q-m) \\ -(t-m)] \end{matrix} \right\}, \end{cases} \tag{7}$$

from which we calculate the difference Δ_{12} between $\Delta 1$ and $\Delta 2$ as follows:

$$\Delta_{12} = -o \cdot [2(r-m) + (t-m)], \tag{8}$$

where r, s, t, and q are high-frequency noises in the positron image, and their DICOM values are all greater than m. Therefore, in Eq. (8), $\Delta_{12} < 0$, $\Delta 2 > \Delta 1$. It can be seen that the use of the convolution kernel shown in Fig. 5(b) for the contrast stretching effect of positron images is better than that shown in Fig. 5(a) and has a certain effect of eliminating or weakening high-frequency noise in the image.

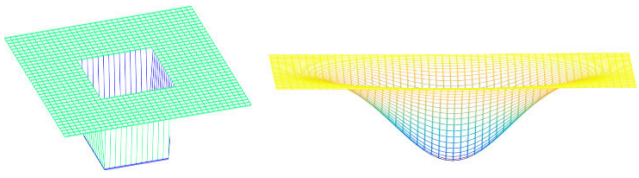

(a) Step mutation (b) Gradual change

FIGURE 6. Schematic of the DICOM value change at the contour.

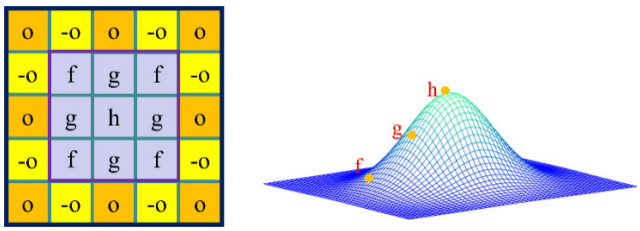

(a) Unequal weight (b) Inner kernel weight

FIGURE 7. Schematic of the weight distribution of the unequal weight convolution kernel and its convolution inner kernel.

The contour feature extraction convolution kernel discussed above is when the DICOM values at the contour are the same and are not affected by the DICOM values of the surrounding non-contour regions. However, in the actual positron image reconstruction process, the DICOM value of a pixel point is determined by the weighted average of the pixel point and its neighboring pixel points. The DICOM value of the pixel is affected by the nuclide activity of the pixel and the DICOM value of the pixel in the neighborhood. Therefore, the DICOM value at the edge of the contour will be higher than the DICOM value at the center of the contour in the positron image. The change in DICOM value from the center of the contour to the contour of the contour edge is not a step change, as shown in Fig. 6(a), but a gradient change, as shown in Fig. 6(b). To solve this problem, the convolution kernel shown in Fig. 7(a) is designed on the basis of the convolution kernel shown in Fig. 5(b).

In the convolution kernel shown in Fig. 7(a), the weights of the convolution inner kernels are distributed according to the distance from the center point of the convolution kernel. That is, $h > g > f$ to weaken the influence of the DICOM value of pixels around the foreign body on the DICOM value of the foreign body area. A suitable convolution inner kernel can be selected approximately according to the Gaussian distribution characteristics shown in Fig. 7(b).

At present, to extract the contour features of a 3D image, a common method is to perform edge detection on the sliced image first and then perform 3D reconstruction on the image after edge detection to obtain the 3D contour feature. This method of contour feature extraction ignores the information between adjacent slices in the positron image, resulting in discontinuities and pseudo contours in the contour features after extraction. In response to the above problems, we will extract the contour features of the positron image from a 3D perspective. The contour features have extension characteristics in different directions in 3D space, in addition to the edge characteristics in the X, Y, and Z directions, as shown in Fig. 8. Consequently, the contour also has edge characteristics in different 45° directions and 135° directions, as shown in Figs. 9 and 10.

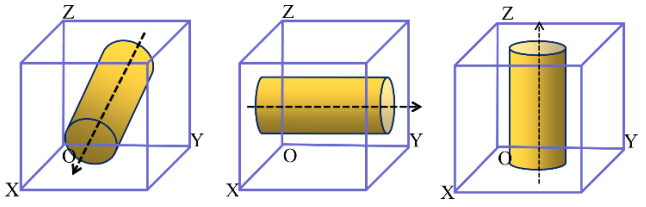

(a) X (b) Y (c) Z

FIGURE 8. Outline extending along the X, Y, and Z directions.

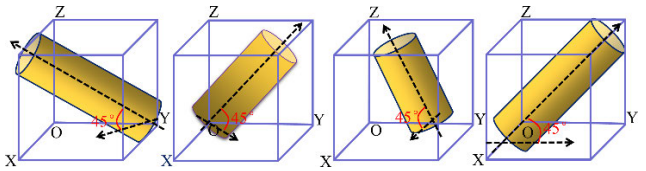

(a) XY45° (b) YX45° (c) XZ45° (d) YZ45°

FIGURE 9. Schematic of the contour extending along different 45° directions in space.

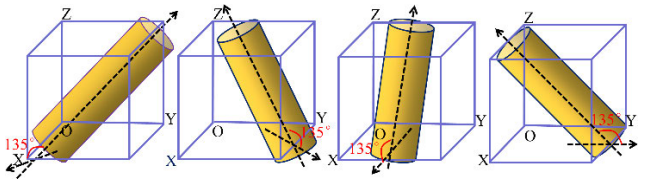

(a) XY135° (b) YX135° (c) XZ135° (d) XY135°

FIGURE 10. Schematic of the contour extending along different 135° directions in space.

To resolve the problem of weak contour edge contrast and high-frequency noise when extracting contour features in a 3D positron image, we construct a 3D anisotropic convolution operator K that can improve image contrast on the basis of the convolution kernel shown in Fig. 7(a). The convolution operator is composed of 3D directed convolution kernels capable of extracting contour features in different extension directions in space. As shown in Fig. 11(a), the 3D directed convolution kernel K_Z has a size of $5 \times 5 \times 3$, which mainly has an extraction effect on contour features extending along the Z direction. The design of the center of the convolution kernel is based on the convolution inner kernel shown in Fig. 7(a). The size is $3 \times 3 \times 3$ and the weights are different, which is used to linearly stretch the image to improve the contour contrast. The remaining parts of the convolution kernel are alternating weights, which are used to extract the contour features by performing differential operations on the image and weaken the influence of noise around the contour.

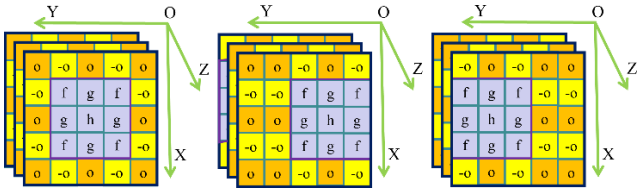

(a) K_Z (b) $K_{YZ45°}$ (c) $K_{YZ135°}$

FIGURE 11. Spatial contour feature extraction convolution kernel.

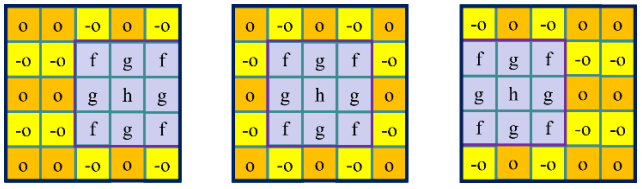

(a) $K_{YZ45°}(:,:,1)$ (b) $K_{YZ45°}(:,:,2)$ (c) $K_{YZ45°}(:,:,3)$

FIGURE 12. Detailed schematic of unequal weight $K_{YZ45°}$.

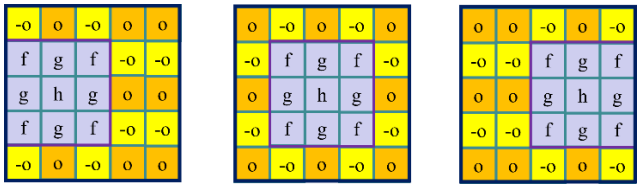

(a) $K_{YZ135°}(:,:,1)$ (b) $K_{YZ135°}(:,:,2)$ (c) $K_{YZ135°}(:,:,3)$

FIGURE 13. Detailed schematic of unequal weight $K_{YZ135°}$.

Given that the contour has extension characteristics in all directions in space, the unidirectional contour feature extraction will lose the contour information in other directions. Therefore, on the basis of the directed convolution kernel K_Z, the directed convolution kernels K_X, K_Y, $K_{XY45°}$, $K_{XY135°}$, $K_{YX45°}$, $K_{YX135°}$, $K_{XZ45°}$, $K_{XZ135°}$, $K_{YZ45°}$, and $K_{YZ135°}$ are designed to extract the contour features of foreign objects along the X and Y directions and the different 45° and 135° directions in 3D space. K_X and K_Y can be obtained by transposing K_Z. The convolution kernels shown in Figs. 11(a) and 11(b) are for YZ45° and YZ135° in the spaces shown in Figs. 9(d) and 10(d), respectively. For other 45° and 135° contour extractions in the space, the directed convolution kernel can be transposed or rotated on the basis of the convolution kernel shown in Figs. 11(a) and 11(b), respectively.

Figs. 12 and 13 respectively show the specific schematics of the 3D directed convolution kernel shown in Figs. 11(a) and 11(b).

The above 3D anisotropic convolution operator K is used for contour feature extraction of positron images. If the contour features are along d (d = X, Y, Z, XY45°, YX45°, XZ45°, YZ45°, XY135°, YX135°, XZ135°, YZ135°) direction has extension characteristics, and when the directional convolution kernel is located in the center of the contour, the above unequal weight directional convolution kernel will have the greatest magnification effect on the DICOM value of the contour. In addition, the multiple is (12f + 12g + 3h), which can improve the contrast at the contour of foreign objects in the image. However, in actual processing, it is not easy to choose a threshold to prevent the DICOM data from being too large after convolution because the convolution kernel is multiplied by the adjustment factor σ, as shown in Eq, (16), by adjusting the value of the adjustment factor σ to achieve the edge gradient magnification. The 3D anisotropic convolution operator K to perform a convolution operation on the positron image and obtain the image feature extraction algorithm in any direction is applied as follows:

$$\begin{cases} K'_d = \sigma \cdot K_d (0 < \sigma < 1, d = X, Y, Z, 45°, 135°) \\ P_d = P \otimes K'_d, \end{cases} \tag{9}$$

where $\otimes$ represents the convolution operation. The convolution obtains the features in different directions and then synthesizes to the result P', 45° represents the set of different 45° directions in space, and 135° represents the set of different 135° directions in space:

$$P' = \sqrt{P_X^2 + P_Y^2 + P_Z^2 + P_{45°}^2 + P_{135°}^2}. \tag{10}$$

To obtain a clear feature image with detailed information, the feature-extracted image P' in Eq. (18) is binarized. After the positron image is processed, the corresponding feature of the area where the feature is located is where the DICOM data are relatively small. However, due to the edge effect of the positron image, the area where the feature is located is not the smallest area. To highlight the features, double threshold processing of the processed data is conducted:

$$G_{ij} = \begin{cases} 1, & T_L < P'_{ij} < T_H \\ 0, & others, \end{cases} \tag{11}$$

where P'_{ij} is an element in the matrix P', and G_{ij} represents an element of the matrix after binarization. T_H is the upper threshold and T_L is the lower threshold.

$$T_L = T_H(1 - \varepsilon), \tag{12}$$

where the value of ε is generally between 1% and 10%. By choosing an appropriate ε, we can effectively eliminate the noise of the positron image and obtain a "clean" feature image after binarization.

III. EXPERIMENT AND IMAGE PROCESSING

A. EXPERIMENTAL DESIGN

The research object of this paper is the hydraulic part made of metal materials, which are shown by the positron image to have curved foreign objects inside. The type of PET detector used is Trans-PET Explorist 180, and the specific parameters of the detector are shown in Table 1.

Fig. 14 shows a diagram of the device under testing, a field test diagram, and a test result diagram. The hydraulic part used in the experiment have a wall thickness of 5 mm and

TABLE 1. Characteristics of Trans-PET Explorist 180.

Parameters	Value
Number of rings	52
Number of crystals per ring	312
Radius of the detection ring	180 mm
Transverse FOV	130 mm
Axial FOV	100 mm
Crystal size	$1.9 \times 1.9 \times 10$ mm^3
Crystal pitch	2.0×2.0 mm^2
Time resolution	1.5 ns
FOV central spatial resolution	0.99 mm
Average energy resolution	15%
Energy window	350–625 keV

(a) Hydraulic part

(b) Test site

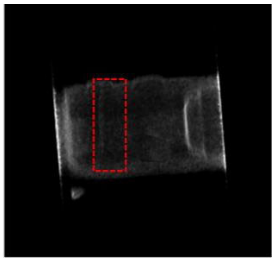

(c) Test result

FIGURE 14. Test process and results of the hydraulic part.

an outer diameter of 73 mm. The material is stainless steel, and the shape is shown in Fig. 14(a). The test hydraulic oil model is HOUGHTO-SAFE 620C. The testing process is as follows: 1) The test is carried out without foreign objects, the F^{18}-labeled radionuclide and the hydraulic oil are fully mixed, and the mixed solution is evenly mixed with a mixer. 2) Approximately 310 mL of the mixed solution is injected into the hydraulic part through the hydraulic hole and into the mixed liquid, and the activity detected during injection is 2.4 mCi. 3) The hydraulic part is fixed in place at the center of the Trans-PET ring detector, and the testing time is 10 min. The obtained data are used as the initial data for the calibration of the detector. 4) The position of the hydraulic part in the detector is kept unchanged a piece of curved metal wire with a diameter of 2 mm is placed in the hydraulic part, and the test result is shown in Fig. 14(c). A total of 10 frames of positron images are obtained according to one frame of image per minute.

B. IMAGE ANALYSIS AND PREPROCESSING

First, a test is carried out without the presence of any foreign objects inside the cavity of the hydraulic part. The effect of the detected data is then observed by frame every 10 min. To observe the detection results, the 150th slice image of

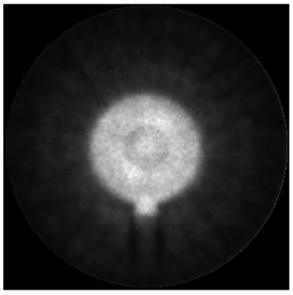

(a) Correction 150th slice

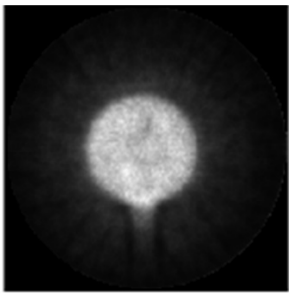

(b) Detection 150th slice

FIGURE 15. Testing result slice.

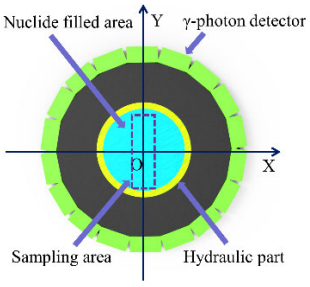

(a) Sampling principle

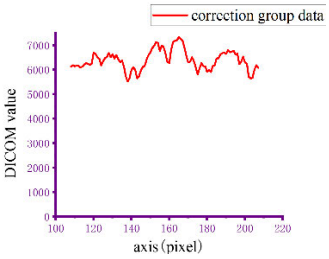

(b) DICOM data curve

FIGURE 16. DICOM data curve of the correction group slice.

the correction group experiment is shown in Fig. 21(a). The reason for taking this slice is that a part of the 2 mm metal wire placed in the subsequent detection experiment is in this area.

As shown in Fig. 15(a), even in the ideal case where no foreign matter is placed, the gray value of the positron image fluctuates from the center to the edge. To reflect the gradient change of the activity value more intuitively, the activity change characteristics of the DICOM data in the sampling area are analyzed according to the sampling method shown in Fig. 16(a). In the case of frame/10 min, the 150th slice of the correction data is selected, and the characteristic curve of the DICOM data from the center to the edge is obtained according to this slice, as shown in Fig. 16(b).

As shown in Fig. 16(b), DICOM data fluctuate even in the area near the detection center because of certain problems, such as photon detector ontology noise, uneven detection efficiency of the multi-channel detector, and photon scattering inside the metal.

Therefore, for the noise in the reconstructed positron image, two different 3D filters, such as bilateral and median filters, are used to process the frame/10 min of the DICOM data. The sizes of the filter are $3 \times 3 \times 3$, $5 \times 5 \times 5$, and $7 \times 7 \times 7$, and the processed result takes the 150th slice of the detection data, as shown in Figs. 17 and 18. Three evaluation indexes, such as PSNR, SSIM, and PTR, are calculated for the 150th slice after different filters and different sizes are filtered, as shown in Tables 2 and 3, respectively.

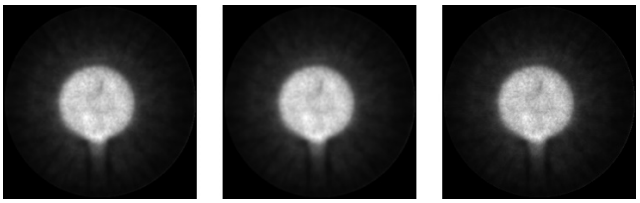

(a) 3 × 3 × 3 (b) 5 × 5 × 5 (c) 7 × 7 × 7

FIGURE 17. Median filter slices of different sizes.

TABLE 2. Evaluation index after filtering by 3D median filter.

Filter size	Evaluation index		
	PSNR	SSIM	PTR
3 × 3 × 3	39.94	0.98	56.44 s
5 × 5 × 5	39.95	0.98	60.22 s
7 × 7 × 7	39.97	0.98	67.24 s

TABLE 3. Evaluation index after filtering by 3D bilateral filter.

Filter size	Evaluation index		
	PSNR	SSIM	PTR
3 × 3 × 3	57.88	0.99	86.17 s
5 × 5 × 5	36.46	0.97	113.22 s
7 × 7 × 7	34.04	0.96	186.85 s

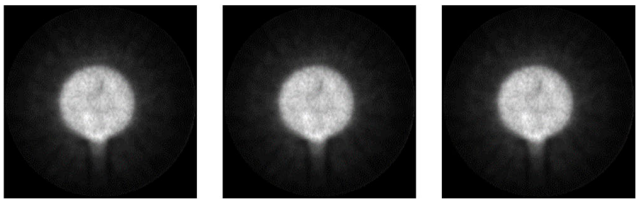

(a) 3 × 3 × 3 (b) 5 × 5 × 5 (c) 7 × 7 × 7

FIGURE 18. Bilateral filter slices of different sizes.

A comparison of the two images after filtering in Figs. 17 and 18 reveals the difficulty of distinguish the filtering effect of different sizes and types of filters in the sensory sense. However, through the PSNR, SSIM, and PTR in Tables 2 and 3, the filtering effect and efficiency of the median filter are shown to be better than those of the bilateral filter. The time cost of the slight improvement in filtering effect caused by increasing the filter size is also very high. According to the method shown in Fig. 16(a), the characteristic curve of the DICOM data from the center to the edge of the detection group data and after the 3D filtering of 3 × 3 × 3 are obtained is shown in Fig. 19. As can be seen from Fig. 19(b), the fluctuation characteristics of DICOM data improved compared those shown in Fig. 19(a). However, due to the inconsistency in detection efficiency of the detector and the asymmetry of the structure and material of the tested object, there are still large fluctuations in the test results that are difficult to eliminate through 3D filtering and smoothing.

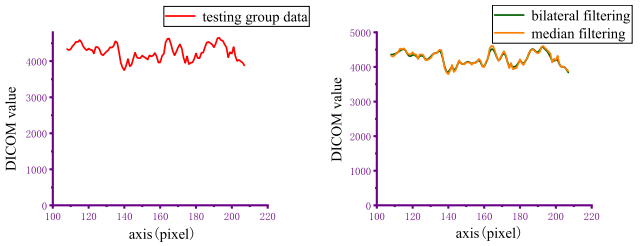

(a) Before filtering (b) After filtering

FIGURE 19. DICOM data curves before and after filtering of the detection group.

In view of the above data fluctuation problem, we propose a full pixel correction algorithm. The principle of the algorithm is that, in the positron image, the nuclide filling part should have the same data under the premise of uniform nuclide distribution and consistent detection efficiency of the detector. The non-nuclide filled part is ignored. For the calibration group experiment, the nuclide distribution in the nuclide-filled area is assumed to be uniform. The reasons for the data fluctuation phenomenon are the asymmetry of the detector structure and the inconsistency of the detector efficiency, which is an inherent feature of the positron detection process. Therefore, the ratio of the data of each pixel in the positron image to the maximum value of the pixel can be used as the correction coefficient, as shown in Eq. (21):

$$w_{ij} = \frac{P_{\max}}{P_{ij}}(i,j) \in w, \tag{13}$$

where w_{ij} represents the correction coefficient for pixel points (i, j) in the experimental group, P_{max} represents the maximum value in one frame of data of the detector, P_{ij} represents the data of pixel points (i, j), and w represents the nuclide-filled area. In actual processing, to avoid errors caused by chance, P_{max} takes the largest N data in the frame data and then averages. After the correction coefficient w_{ij} is obtained, point-to-point correction is performed on the detection data containing foreign objects, as shown in Eq. (22):

$$H'_{ij} = H_{ij} \cdot w_{ij}, \tag{14}$$

where H'_{ij} represents the corrected value of the pixel point (i, j) in the foreign object experiment group, and H_{ij} is the value before correction. Combined with Eq. (22), point-to-point correction is performed on the detection group data after 3D median filter processing, and the 150th slice is taken as shown in Fig. 20.

A comparison of Fig. 20 with Fig. 17(a) illustrates that, in the slice 150 image, the cross-sectional profile of the metal foreign body is vaguely seen (marked in the box in Fig. [20]).

C. FOREIGN BODY CONTOUR FEATURE EXTRACTION

After the 3D filtering and full pixel correction of the positron image, part of the image noise is removed and the contour features of foreign objects in the image are slightly enhanced. However, the image still has the problems of unobvious

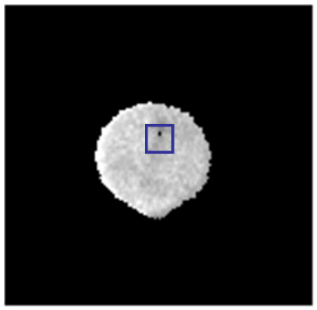

FIGURE 20. Detection group 150th slice after correction.

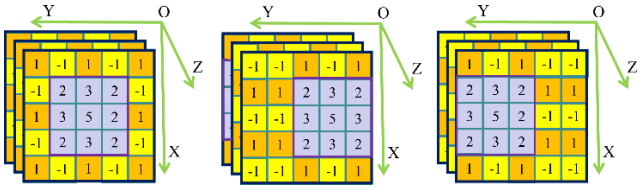

FIGURE 21. Contour kernel for contour extraction of foreign objects with unequal weight.

FIGURE 22. 150th slice after contour feature extraction of foreign objects with unequal weight.

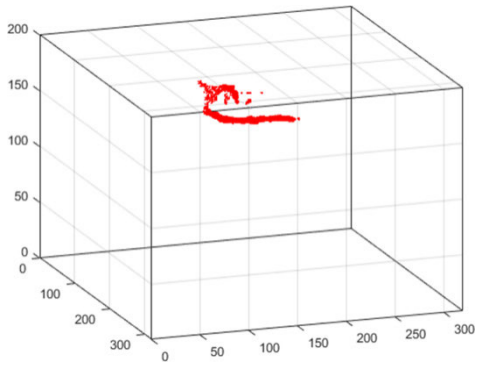

FIGURE 23. Scatter plot after binarization.

contour features and excessive noise around the contour. As the detection object is a linear foreign object contour, to better extract the contour features of the foreign object in the positron image, this research proposes a 3D anisotropic convolution operator that uses this operator to perform convolution operations on the image. The contrast between the foreign objects and the surroundings is pulled apart to highlight the contour characteristics of the foreign objects.

In the experiment, according to the pixel size of the positron image and the size of the metal foreign body, a 3D anisotropic convolution operator with unequal weights is designed on the basis of Fig. 11 to extract the contour features of the corrected positron image, o = 1, f = 2, g = 3, and h = 5, in the convolutional kernel. Fig. 21 shows the 3D directed convolution kernels K_Z, $K_{YZ45°}$, and $K_{YZ135°}$ in the unequal-weight 3D anisotropic convolution operator that can extract foreign object contours along the Z, YZ45°, and YZ135° directions. The directional convolution kernel for extracting foreign object contours extending in the X and Y directions and other 45° and 135° directions in space can be obtained by transposing or rotating the above three directional convolution kernels. For the 3D directed convolution kernel shown in Fig. 21, when the contour of the foreign body coincides with it, the DICOM value of the foreign body contour has a maximum magnification effect of 75 times.

To facilitate the observation and comparison of operation results, the values of the adjustment factors are set to 0.02 and 0.03, respectively. Data mapping processing is performed on the convolved DICOM data according to the adjustment factor. When the adjustment factor is 0.02, the data in the range of 26000–34000 is mapped to the grayscale variation range of 0–255. The grayscale image of the 150th slice after data mapping is shown in Fig. 22(a). The adjustment factor is 0.03, and the data in the range of 39000–51000 are mapped to the grayscale variation range of 0–255. The grayscale image of the 150th slice after the data mapping process is shown in Fig. 22(b).

Comparing (a) and (b) in Fig. 22 reveals that the effect of different adjustment factors on the extraction of the foreign body profile is not obvious. The difference is that the selection of different adjustment factors can change the magnification of the DICOM data gradient between the foreign body and its surroundings. The selection of the appropriate impact factor makes it possible to select the mapped DICOM data range more intuitively and clearly in the above mapping process. Observe the DICOM data in Fig. 22(a) and analyze the change of DICOM data near the edge of the foreign object. The contour and dark spots of this area are obvious. Hence, the values of the bright and dark spots in the area are used as the basis for obtaining the contour. With Fig. 22(a) taken as an example in this study, the selected threshold is [27500, 30000], and the data are binarized according to the threshold and drawn into a scatter plot as shown in Fig. 23.

The scatter in Fig. 23 reveals the contour characteristics of foreign objects, but there is still a small amount of noise around. Given that the foreign objects in the experiment are linear objects with a certain length and diameter, this study extracts a 3D scatter filter to eliminate noise. The algorithm principle is as follows: design a 3D scatter filter, the size

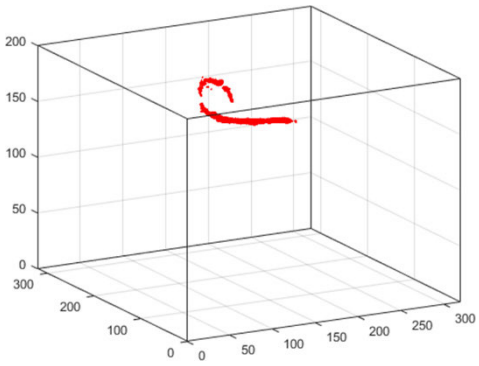

FIGURE 24. Scatter plot after 3D scatter filtering.

of which is M×N×P and depends on the actual detection the situation. The 3D scatter filter traverses the 3D scatter diagram shown in Fig. 23 and calculates the number T of pixels with non-zero pixel values in the filter window at this time. In addition, the coefficient q is calculated as Eq. (15):

$$q = \frac{T}{M \cdot N \cdot P}, \tag{15}$$

where the coefficient q is obtained through the above calculation, and a threshold value q_{th} is set to distinguish between foreign objects and noise. If $q > q_{th}$, then it is a foreign object; otherwise, it is noise. Through the above processing method, the result shown in Fig. 24 is obtained, and the coefficient adjusted according to the size of the foreign body is $M = N = P = 3$, $q_{th} = 0.7$.

It can be seen from Figure 24 that the contour feature of the foreign body is very obvious, but there is the problem of discontinuous contour feature. To solve the above problem, this paper uses a 3D path search algorithm to obtain the centroid coordinate set of the contour feature, and then performs a 3D curve fitting on the centroid coordinate set to obtain a smooth and continuous contour feature. Figure 25(a) shows the result of curve fitting. To more accurately reflect the position information of foreign objects in the hydraulic part, the positron DICOM data corresponding to the contour of the curve are also feature-enhanced. The processed positron image and 3D SolidWorks image of the hydraulic part are matched and synthesized as shown in Fig. 25(b). This figure clearly shows the shape and position of linear foreign objects in the hydraulic part. Compared with Fig. 14(c), Fig. 25(b) can show the outline characteristics of the foreign body more clearly and completely. Furthermore, the curved part of the front end of the foreign body that is difficult to observe in other software can be clearly displayed after processing. According to the coordinate deviation of the foreign body pixels before and after extraction combined with the calculation of the image pixel size, the extracted position deviation is 1 mm.

To verify the versatility of the method proposed in this study, the linear foreign objects inside the cavity of the hydraulic part shown in Fig. 14(a) were detected. The diameter of the linear foreign object is 2 mm, and the hydraulic

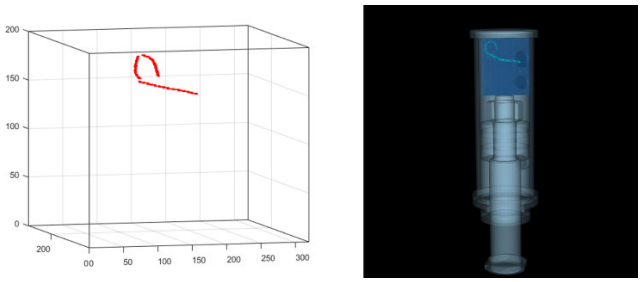

(a) Fitted scatter plot (b) Matched image

FIGURE 25. Scatter plot after 3D fitting and image after 3D matching.

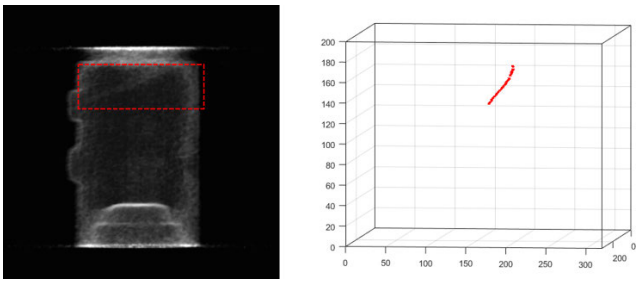

(a) Testing result (b) Processed 3D scatter plot

FIGURE 26. Straight-line foreign object testing image and processed 3D scatter plot.

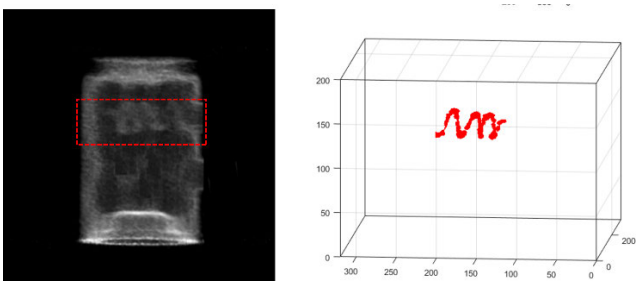

(a) Testing result (b) Processed 3D scatter plot

FIGURE 27. Image after the testing of the spiral foreign object and the processed 3D scatter plot.

oil mixture with an activity of 2.13 mCi is injected for a detection time of 10 min. The detected positron image is shown in Fig. 26(a), and Fig. 26(b) is the outline extracted after processing. To verify the effect of the method proposed in this study on the extraction of complex edge contours, the spiral foreign object inside the cavity of the hydraulic part was tested. The diameter of the foreign object is 2 mm, and the hydraulic oil mixture with an activity of 1.93 mCi is injected. The detected positron image is shown in Fig. 27(a). Fig. 27(b) is the outline extracted after processing.

To verify that the proposed algorithm has the extraction effect on the contour features of different metal cavity, the hydraulic part shown in Figure. 28(a) is also designed to verify the algorithm, and the test site is shown in Fig. 28(b). The hydraulic part used in the experiment have a wall thickness

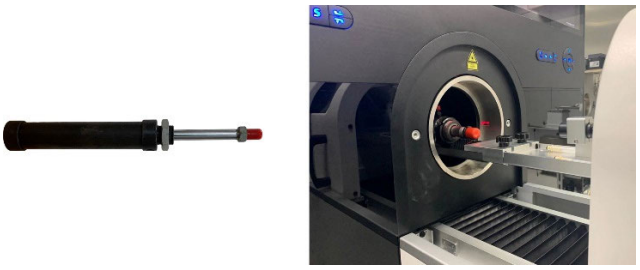

(a) Hydraulic part (b) Test site

FIGURE 28. Test process and the hydraulic part.

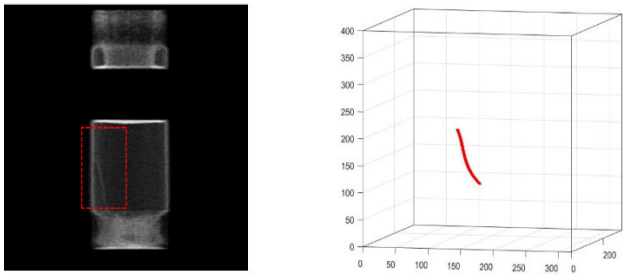

(a) Testing result (b) Processed 3D scatter plot

FIGURE 29. Image after the testing of the linear foreign object and the processed 3D scatter plot.

of 5 mm, the outer diameter is 53 mm, the material is alloy steel, and the diameter of the linear foreign object is 2 mm. The test hydraulic oil model is HOUGHTO-SAFE 620C, and the type of PET detector used is Trans-PET Explorist 180. During the experiment, about 200 ml of nuclide mixture is injected, the activity detected during injection is 2.1 mCi, the detection time is 10 min. The detected positron image is shown in Fig. 29(a), Fig. 29(b) is the outline extracted after processing.

IV. CONCLUSION

This research aims to apply the positron injection method for state detection inside the closed metal cavity and design the 3D anisotropic convolution operator for the contour feature extraction problem inside the cavity. In actual testing, the imaging inside the metal cavity and the extraction of the contour features of the foreign objects inside the cavity are realized. Research results show that the algorithm proposed in this study can extract and display the contour features inside the cavity well in the positron image with low resolution, low contrast, and low SNR, which proves that positron annihilation technology in the industry field of non-destructive testing has good development prospects. Aiming at the problem of positron image noise caused by inconsistent detectors and metal scattering effects, an image preprocessing algorithm combining filtering and full pixel correction is proposed. In the process of feature extraction, the 3D anisotropic convolution operator proposed in this paper fully considers the problem of low image edge contour contrast and difficulty in extracting due to the volume effect in the positron image reconstruction process, and the spatial orientation of the operator also has a certain directional filtering effect; To solve the contour feature discontinuity in the extracted contour feature, a 3D path search algorithm is proposed to obtain the centroid coordinate set of the contour feature, and then the centroid coordinate set is subjected to 3D curve fitting to obtain a smooth and continuous contour feature. The results in this paper also show that filtering and convolution of the positron image in 3D have good effects. In the processing of positron data, processing DICOM data directly avoids problems such as loss of details owing to data compression during data conversion. This study addresses the imaging and foreign object detection methods in dense metal cavities and provides new research ideas for non-destructive testing of metal cavities, such as pipes and hydraulic part in industrial equipment.

REFERENCES

[1] J. T. Liu, M. Zhao, H. Xiao, and M. Yao, "Investigation of non-destructive testing in inner cavity with ant-nest structure based on positron annihilation," *Defect Diffusion Forum*, vol. 373, pp. 61–64, Mar. 2017, doi: 10.4028/www.scientific.net/DDF.373.61.

[2] M. Yao, Y. Q. Zhang, M. Zhao, R. P. Guo, and J. Xu, "Research on combustion flow field imaging method based on ray casting algorithm," *AIP Adv.*, vol. 9, no. 5, May 2019, Art. no. 055022, doi: 10.1063/1.5042043.

[3] H. Xiao, M. Zhao, J. Liu, and H. Chen, "A study on scattering correction for γ-photon 3D imaging test method," *AIP Adv.*, vol. 8, no. 3, Mar. 2018, Art. no. 035315, doi: 10.1063/1.5022486.

[4] H. Xiao, M. Zhao, J. T. Liu, J. Liu, and H. Chen, "A new method for spatial structure detection of complex inner cavities based on 3D γ-photon imaging," *AIP Adv.*, vol. 8, no. 5, May 2018, Art. no. 055205, doi: 10.1063/1.4984027.

[5] F. Chiti, S. Bakalis, W. Bujalski, M. Barigou, A. Eaglesham, and A. W. Nienow, "Using positron emission particle tracking (PEPT) to study the turbulent flow in a baffled vessel agitated by a rushton turbine: Improving data treatment and validation," *Chem. Eng. Res. Des.*, vol. 89, no. 10, pp. 1947–1960, Oct. 2011, doi: 10.1016/j.cherd.2011.01.015.

[6] I. I. Bardyshev, Y. P. Toporov, V. A. Klyuev, A. V. Gol'danskii, and V. A. Kotenev, "On diagnostics of double electric layer in the zone of metal–polymer adhesion contact using the Positron-Annihilation-Probe method," *Protection Met. Phys. Chem. Surf.*, vol. 53, no. 6, pp. 1181–1186, Nov. 2017, doi: 10.1134/S2070205117060053.

[7] K. Cole, P. R. Brito-Parada, A. Morrison, I. Govender, A. Buffler, K. Hadler, and J. J. Cilliers, "Using positron emission tomography (PET) to determine liquid content in overflowing foam," *Chem. Eng. Res. Des.*, vol. 94, pp. 721–725, Feb. 2015, doi: 10.1016/j.cherd.2014.10.014.

[8] Z. C. Zhang, "The filtering and streamline of three-dimensional point-cloud data," *Appl. Mech. Mater.*, vols. 511–512, pp. 554–558, Feb. 2014, doi: 10.4028/www.scientific.net/amm.511-512.554.

[9] L. Li, "Research on 3D ultrasonic image filtering method based on GPU acceleration," M.S. thesis, Dept. Sci. Technol., Hust Univ., Hubei, China, 2014.

[10] J. Du, S. B. Fain, T. Gu, T. M. Grist, and C. A. Mistretta, "Noise reduction in MR angiography with nonlinear anisotropic filtering," *J. Magn. Reson. Imag.*, vol. 19, no. 5, pp. 632–639, May 2004, doi: 10.1002/jmri.20047.

[11] Y. H. Zeng and M. Gao, "Research on wavelet adaptive threshold method based on Bayesian estimation for image denoising," *J. Biomed. Eng. Res.*, vol. 37, no. 4, pp. 410–413, Dec. 2018, doi: 10.19529/j.cnki.1672-6278.2018.04.07.

[12] R. Albano, "Investigation on roof segmentation for 3D building reconstruction from aerial LIDAR point clouds," *Appl. Sci.*, vol. 9, no. 21, Sep. 2019, Art. no. 4674, doi: 10.3390/app9214674.

[13] N. Nomura and N. Hamada, "Feature edge extraction from 3D triangular meshes using a thinning algorithm," presented at the Conf. Vis. Geometry X, San Diego, CA, USA, Jul. 2001.

[14] X. Zhang and E. Y. Lam, "Edge detection of three-dimensional objects by manipulating pupil functions in an optical scanning holography system," presented at the IEEE Int. Conf. Image Process., Hong Kong, Sep. 2010.

TAO JIANG was born in Anqing, Anhui, China, in 1995. He received the B.Sc. degree from the Beijing Information Science and Technology University, China, in 2014. He is currently a Graduate Student with the Nanjing University of Aeronautics and Astronautics. His research interests include positron nondestructive testing, algorithm optimization, and image processing.

MIN ZHAO is a Professor and a Doctoral Supervisor with the Nanjing University of Aeronautics and Astronautics. He is currently a member of the Metrology Technology Professional Committee, Chinese Society of Aeronautics and Astronautics; the Vice Chairman of the Thermal Engineering Professional Committee, Jiangsu Institute of Metrology and Testing; and the Chairman of the Supervisory Board, Jiangsu Institute of Instrumentation. His current research interests include UAV trajectory planning and control, positron annihilation technology for nondestructive testing, computer measurement, and control system for high-speed railway nondestructive testing.

MIN YAO received the B.Sc., M.Sc., and Ph.D. degrees from the Nanjing University of Aeronautics and Astronautics, China, in 1997, 2002, and 2008, respectively. She is currently an Associate Professor with the Nanjing University of Aeronautics and Astronautics. Her research interests include computer measurement, control and UAVs task assignment, data and signal processing, and algorithm optimization.

RUIPENG GUO received the Ph.D. degree in instrument science and technology from Shanghai Jiaotong University, Shanghai, China, in 2011. She is currently an Associate Professor with the Nanjing University of Aeronautics and Astronautics. Her research interests include nondestructive testing, computer measurement, as well as control and signal processing.

TONG SUN was born in Huaian, Jiangsu, China, in 1995. He received the B.Sc. degree from Yang Zhou University, China, in 2014. He is currently a Graduate Student with the Nanjing University of Aeronautics and Astronautics. His research interests include positron nondestructive testing, algorithm optimization, and image processing.

ZENGHAO ZHAO received the B.Sc. degree from the Jinling University of Science and Technology, in 2018. He is currently a Graduate Student with the Nanjing University of Aeronautics and Astronautics. His main research interests include detection technology and signal processing.

HUI XIAO received the Ph.D. degree from the College of Automation Engineering, Nanjing University of Aeronautics and Astronautics (NUAA), Nanjing, China, in 2020. He holds a postdoctoral position with the College of Computer Science and Technology, NUAA. He is currently with the NUAA Shenzhen Research Institute. His main research interests are photon imaging testing technology and 3-D image reconstruction algorithms based on AI.

YUHUI LI was born in Luonan, Shaanxi, China, in 1995. He received the B.Sc. degree from the Nanjing University of Aeronautics and Astronautics, China, in 2018, where he is currently pursuing the M.Sc. degree. His main research interests include parafoil system modeling, trajectory planning, and control.